Research Article

OPTICA QUANTUM

Quantum interferences and gates with emitter-based coherent photon sources

I. Maillette de Buy Wenniger,[1,2,†,*] S. C. Wein,[3,†] D. Fioretto,[2] S. E. Thomas,[2] C. Antón-Solanas,[4] A. Lemaître,[1] I. Sagnes,[1] A. Harouri,[1] N. Belabas,[1] N. Somaschi,[3] P. Hilaire,[3] J. Senellart,[3] and P. Senellart[1,3]

[1]Université Paris-Saclay, CNRS, Centre for Nanosciences and Nanotechnology, 91120 Palaiseau, France
[2]Department of Physics, Imperial College London, London SW7 2BW, UK
[3]Quandela SAS, 10 Boulevard Thomas Gobert, 91120 Palaiseau, France
[4]Departamento de Física de Materiales, Instituto Nicolás Cabrera, Instituto de Física de la Materia Condensada, Universidad Autónoma de Madrid, 28049 Madrid, Spain
[†]These authors contributed equally to this work.
*imaillet@ic.ac.uk

Received 16 April 2024; revised 20 September 2024; accepted 8 October 2024; published 13 November 2024

Quantum emitters such as quantum dots, defects in diamond or in silicon have emerged as efficient single-photon sources that are progressively exploited in quantum technologies. In 2019, it was shown that the emitted single-photon states often include coherence with the vacuum component. Here we investigate how such photon-number coherence alters quantum interference experiments that are routinely implemented both for characterizing or exploiting the generated photons. We show that it strongly modifies intensity correlation measurements in a Hong–Ou–Mandel experiment and leads to errors in indistinguishability estimations. It also results in additional entanglement when performing partial measurements. We illustrate the impact on quantum protocols by evidencing modifications in heralding efficiency and fidelity of two-qubit gates.

Published by Optica Publishing Group under the terms of the Creative Commons Attribution 4.0 License. Further distribution of this work must maintain attribution to the author(s) and the published article's title, journal citation, and DOI.

https://doi.org/10.1364/OPTICAQ.527420

1. INTRODUCTION

Single quantum emitters such as atoms, defects in diamond, molecules or quantum dots are natural deterministic single-photon emitters [1–7]. They can be brought to their excited state and emit single photons with near-unity probability. Their spontaneous emission can be efficiently funneled into a single optical mode by making use of the Purcell effect when they are inserted in optical cavities. Together with coherent excitation schemes [8–14], these methods have allowed the demonstration of single-photon sources with a very high degree of indistinguishability and efficiencies orders of magnitude higher than heralded single-photon sources based on frequency conversion [15], making them great assets to scale-up optical quantum technologies [16]. In particular, quantum dot (QD) based single-photon sources are now commercially available and are exploited for quantum computing protocols, enabling a significant increase in the number of manipulated qubits, both on chip and in free space [17–23].

In 2019, it was shown that, when coherently driven, such quantum emitters can directly generate light wave packets consisting of arbitrary quantum superpositions of zero and one photon [24], in other words *single-rail qubits*. The coherent excitation creates a superposition between the ground and excited state of the two-level system that, upon spontaneous emission, is transferred to the electromagnetic field. Such deterministic and efficient generation of single-rail qubits could be of great value for quantum technologies. Indeed, superpositions of zero- and one-photon Fock states are a widely studied resource in photonic information processing [27,28] as well as quantum communication protocols [29–31]. It is important to note that, so far, most of these protocols have been implemented either using weak coherent states [29–31] or by interfering single photons with squeezed coherent states [27,32,33]. However, such approaches carry strong limitations arising from higher order Fock state components, limiting the scalability of the envisioned protocols [34].

The demonstration of deterministic generation of coherent superposition of zero and one photon [24] has recently opened the path toward a more scalable exploitation of single-rail qubits as well as new tailored protocols. Indeed, applications in quantum technologies are progressively emerging, with propositions of application to quantum key distribution [35], Boson sampling [36], interfacing single- and dual-rail optical qubits [28], as well as the very first experimental studies [21].

In the present work, we revisit Hong–Ou–Mandel (HOM) interference to analyze and understand the effect of coherence with vacuum in linear quantum protocols that are used both for characterizing light emitted by quantum emitters as well as for manipulating quantum information. Hence, our work is intended

both for the community of researchers developing single-photon sources based on quantum emitters and for those exploiting these sources for quantum information processing. We first show that coherence with vacuum can lead, and has led, to errors in the measurement of photon indistinguishability for emitter-based single-photon sources. We then explain how it leads to specific quantum interference patterns when performing partial measurements on multiple light pulses, and generates additional entanglement. Considering that partial measurements are central to the scalability of quantum computing, we numerically study the impact of coherence with vacuum on heralded two-qubit gates. Our findings suggest that tailored quantum information processing protocols can be derived to exploit the deterministic generation photon-number superposition with quantum emitters.

The present manuscript is organized as follows. In Section 2, we recall the formalism of HOM interference with true single-photon states and how it can be used to measure the indistinguishability of the single-photon wave packets. To provide a reference, we experimentally illustrate this well-known situation using a quantum dot-based single-photon source under incoherent excitation. In Section 3, we study the impact of coherence with vacuum on HOM interference and evidence the emergence of multiple phenomena. We first evidence the observed experimental signatures on a coherently driven quantum dot (Section 3.1) and demonstrate how the intensity correlation measurement should be revised (Section 3.2). Section 4 discusses the errors in indistinguishability measurements that can arise in the characterization of quantum emitter-based single-photon sources from this overlooked coherence with vacuum. In Section 5, we analyze another feature of HOM interference and evidence how coherence with vacuum leads to additional entanglement when performing partial measurements. Finally, in Section 6, we numerically illustrate how such coherence impacts quantum computing protocols by analyzing the case of a heralded control-NOT (CNOT) gate, i.e., a dual-rail encoded protocol fed with wave packets constituting superpositions of zero and one photons.

2. HONG–OU–MANDEL INTERFERENCE FOR INDISTINGUISHABILITY MEASUREMENTS

Quantifying the degree of indistinguishability of photons emitted by an (artificial) atom is critical to develop useful quantum light sources for quantum technologies. A typical test is the ability of the quantum emitter to successively emit identical single-photon pulses. We illustrate the typical implementation for performing such indistinguishability measurements in Fig. 1(a). A stream of light pulses separated in time by τ_p, with $1/\tau_p$ being the repetition rate of the excitation laser, are sent to the input of a path-unbalanced Mach–Zehnder interferometer, where delayed wave packets are temporally overlapped at the final beam splitter BS_2. Single-photon detectors, D_1 and D_2 monitoring the two outputs, register both single and coincidence counts. The relative polarization of the photons entering the last beam splitter is controlled by a half-wave plate ($\lambda/2$) on one input of BS_2. Two measurements are then performed: one with parallel ($\|$) polarization for both input fields, i.e., where the photons are made as identical as possible in all degrees of freedom, and one with orthogonal ($\perp$) polarization where no interference takes place.

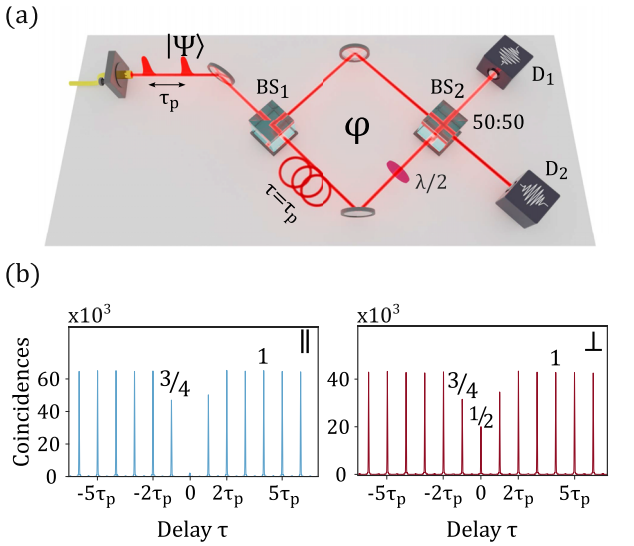

Fig. 1. (a) Experimental setup to perform Hong–Ou–Mandel interference between two consecutively emitted photonic states (τ_p = 12.3 ns) at a 50 : 50 beam splitter (BS_2), where two detectors D_1 and D_2 measure coincidences at the output. The photonic states pick up a relative phase φ when passing through the interferometer. The half-wave plate $\lambda/2$ determines parallel or orthogonal polarization of the two arms in the interferometer. (b) Coincidence histograms for parallel ($\|$) and perpendicular ($\perp$) polarization interference configuration for incoherent pulsed excitation of the emitter via phonon-assisted excitation, so that coherence with vacuum is negligible.

We recall the standard experimental features of HOM interference with single-photon states. To do so, we use a semiconductor QD inserted in a microcavity pillar as described in Refs. [6,37]. We use here an excitation scheme that does not generate coherence with vacuum. It relies on phonon-assisted excitation that has been shown to maintain near-unity indistinguishability while providing an incoherent population transfer of the quantum emitter [38–40]

Figure 1(b) presents the two detector cross correlation histograms in parallel and orthogonal configuration under such excitation. Each peak in these histograms corresponds to a correlation measurement with respect to different delays between photons detected by the two detectors, $\tau = k\tau_p$ for integer k. The absence of coincidence counts in the $k = 0$ delay peak for the parallel configuration indicates the quantum interference of perfectly indistinguishable single photons, where both photons bunch at the output of the final beam splitter. When the indistinguishability is imperfect, the area of the zero delay peak gives access to the mean wave packet overlap M, quantifying the indistinguishability.

In the limit of high loss, the coincidence histograms give access to intensity correlation functions, since the probability of detection becomes proportional to the average photon-number at the detector. The area of the zero delay peak in the parallel polarization configuration is proportional to

$$G^{(2)}_{D_1,D_2,\|}(k=0) = \frac{1}{4}\iint G^{(2)}_{D_1,D_2,\|}(t_1,t_2)\,dt_1\,dt_2, \qquad (1)$$

where $G^{(2)}_{D_1,D_2,\|}(t_1,t_2) = \langle \hat{a}_1^\dagger(t_1)\hat{a}_2^\dagger(t_2)\hat{a}_2(t_2)\hat{a}_1(t_1)\rangle$ is the unnormalized two-time second-order intensity correlation function for

detectors D_1 and D_2 with detection times t_1 and t_2 monitoring the output modes described by photon annihilation operators $\hat{a}_1$ and $\hat{a}_2$, respectively. The integrals are taken over the duration of a single pulse. The *normalized* correlation function then reads

$$g^{(2)}_{D_1,D_2,\parallel}(k=0) = \frac{4}{\mu^2} G^{(2)}_{D_1,D_2,\parallel}(k=0), \tag{2}$$

where $\mu/2$ is the average photon-number in each input port of the final 50:50 beam splitter BS_2.

In practice, the experimental normalization procedure provides absolute values of intensity correlation functions without knowledge on the transmission and efficiency of every component in the experimental setup—a difficult task that falls into the category of metrology. One way to obtain the normalized intensity correlation function is to integrate the coincidences over the duration of the measurement and subsequently normalizing by the product of the total single detection probabilities measured by each detector. Equivalently, one can simply normalize the area of the zero delay peak by the area of the far delay peaks of the correlation histogram either in parallel or perpendicular configuration $G^{(2)}_{D_1,D_2,\parallel(\perp)}(|k| \geq 2)$ since

$$\begin{aligned} G^{(2)}_{D_1,D_2,\perp}(|k| \geq 2) &= G^{(2)}_{D_1,D_2,\parallel}(|k| \geq 2) \\ &= \iint I_1(t_1) I_2(t_2)\, dt_1\, dt_2 = \frac{\mu^2}{4}, \end{aligned} \tag{3}$$

where $I_i(t) = \langle \hat{a}_i^\dagger(t) \hat{a}_i(t) \rangle$ is the average intensity at detector D_i, and $\mu_i = \mu/2$ for balanced beam splitters BS_1 and BS_2. After normalization, the area of the coincidence peaks for $|k| \geq 2$ is 1 and the single-photon indistinguishability M is obtained via the HOM visibility defined as [41,42]

$$V_{HOM} = 1 - \frac{g^{(2)}_{D_1,D_2,\parallel}(k=0)}{g^{(2)}_{D_1,D_2,\perp}(k=0)}, \tag{4}$$

where $g^{(2)}_{D_1,D_2,\parallel(\perp)}(k=0)$ is the *normalized* second-order intensity correlation for zero delay between detectors in parallel (orthogonal) configuration. As an example, from the experimental data shown in Fig. 1(b), we deduce a total mean wave packet overlap $M = V_{HOM} = (91.66 \pm 0.26)\%$ using this approach.

A last typical feature of the normalized experimental peaks is the area of the $|k| = 1$ peak that amounts to 3/4. This can be understood considering the number of ways a pulse sequence of single photons can contribute to each peak [43]. There are three unique paths for the photons to take that contribute to the $|k| = 1$ peak, each with the same probability of occurring when considering balanced beam splitters. However, for the $|k| \geq 2$ peaks, there are four possible paths and hence the observed normalized peak ratio of 3/4.

3. EFFECT OF COHERENCE WITH VACUUM ON HONG–OU–MANDEL INTERFERENCE

We now revisit HOM interference with single-photon wave packets showing quantum coherence with vacuum. We first evidence the multiple experimental signatures arising from coherence with vacuum, provide the theoretical framework to account for these observation, and explain how to adapt the experimental protocol accordingly.

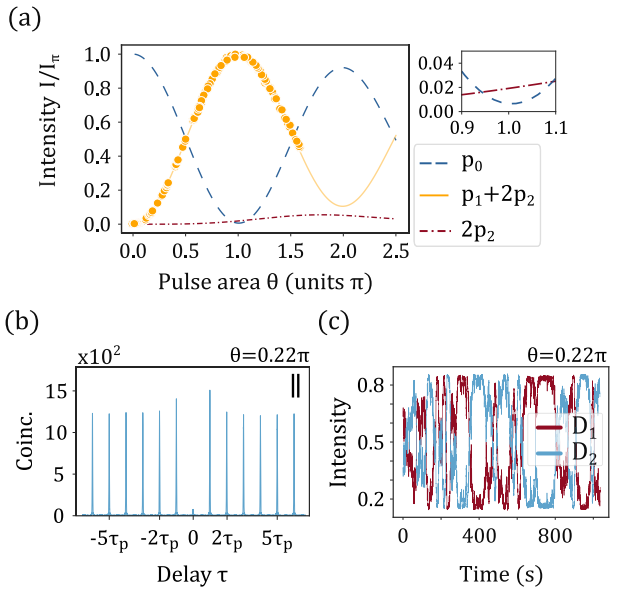

Fig. 2. (a) Measured QD emission intensity (yellow dots) as a function of pulse area θ of the resonant driving laser shows the onset of Rabi oscillations. Also shown are the theoretical fit to the data (yellow line) using a simple two-level system model, and the corresponding predictions for zero-photon probability (blue dashed) and the two-photon contribution to the emission intensity (red dash-dotted). The curves are normalized to the maximum emission intensity I_π (at $\theta = \pi$). The inset shows the zero- and two-photon predictions near $\theta = \pi$. (b) Two-time second-order correlation histogram for an emitter driven with pulse area $\theta = 0.22\pi$ in parallel polarization configuration. (c) Intensities measured by detectors D_1 and D_2 in a Hong–Ou–Mandel setup for a resonantly driven emitter with pulse area $\theta = 0.22\pi$, showing anticorrelated oscillations as a function of the freely evolving phase φ.

3.1. Experimental Signatures

To generate a quantum superposition of zero and one photon, we exploit a resonant excitation scheme, the most widely used excitation technique to obtain indistinguishable single photons. In practice, the laser is resonant to the QD transition and the emitted light is separated from the laser using a cross-polarization configuration [6]. Figure 2(a) shows the emission intensity I as a function of pulse area θ (yellow circles) normalized by the emission intensity at $\theta = \pi$, evidencing the onset of Rabi oscillations. Figure 2(b) shows the coincidence peaks in parallel configuration measured for pulse area $\theta = 0.22\pi$. While the coincidence peaks for $\theta = \pi$ appear close to the case of incoherent excitation (not shown), distinct differences in relative peak heights are observed for $\theta = 0.22\pi$. Notably, the area of the $|k| = 1$ peaks is greater than the area of the $|k| \geq 2$ peaks. Another important signature of photon-number coherence is observed when considering the single counts on each detector [24]. Figure 2(c) evidences that the single counts slowly fluctuate over time in opposite phase, indicating the presence of substantial photon-number coherence for $\theta = 0.22\pi$.

As demonstrated in Ref. [24], for sources with negligible multi-photon emission, the coherence between the ground and excited state imprinted by the laser is transferred to the electromagnetic field through spontaneous emission [25]. The resulting

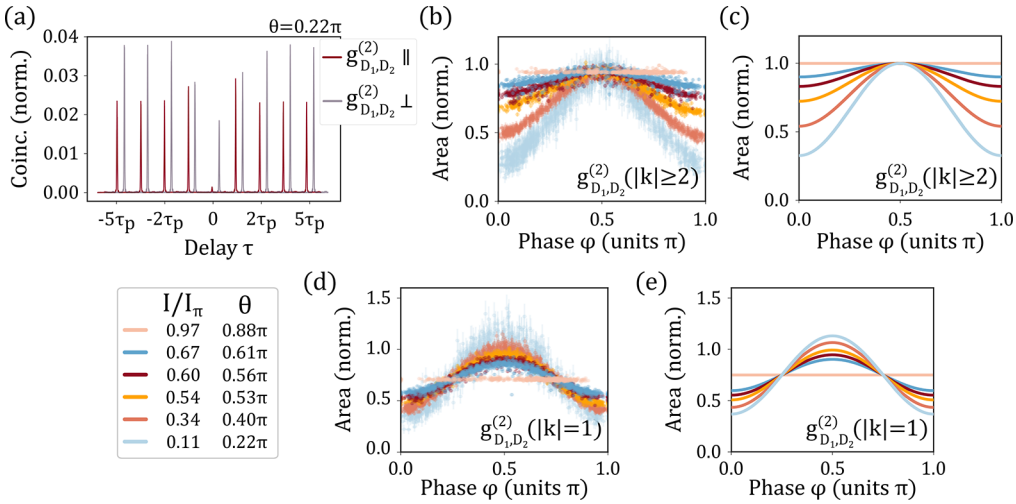

Fig. 3. (a) Integrated coincidence histograms in parallel (red) and orthogonal (grey) polarization configuration for $\theta = 0.22\pi$ normalized using the phase-independent normalization factor (see main text). The delay axis of the grey curve is shifted for clarity. (b) Experimentally extracted normalized areas of the $|k| \geq 2$ peaks from phase-resolved coincidence histograms $g^{(2)}_{D_1,D_2,\parallel}$ as a function of optical phase φ and pulse area $\theta = 2\arcsin(I/I_\pi)$. (c) Theoretical prediction of the normalized far delay peak areas ($|k| \geq 2$) as a function of optical phase φ and pulse area. (d) and (e) Same as in panels (b) and (c), respectively, but for the $|k| = 1$ peak areas.

state of light is then well described by

$$|\Psi(\theta,\alpha)\rangle = \cos\left(\frac{\theta}{2}\right)|0\rangle + e^{i\alpha}\sin\left(\frac{\theta}{2}\right)|1\rangle, \tag{5}$$

where the phase α is imposed by the laser. The pulse area allows for tuning of the zero- ($p_0 = \cos^2(\theta/2)$) and one- ($p_1 = \sin^2(\theta/2)$) photon populations and photon-number coherence $\rho_{01} = e^{i\alpha}\sin\left(\frac{\theta}{2}\right)\cos\left(\frac{\theta}{2}\right)$. In our experiment, the interferometer is not actively stabilized and the two wave packets pick up a slowly varying relative phase φ, i.e., the amplitude of light in one arm experiences a phase shift $\alpha \rightarrow \alpha + \varphi$, leading to phase-dependent quantum interference at beam splitter BS_2. The single counts $I_{1,2}$ measured by detectors $D_{1,2}$ are now proportional to

$$I_{1,2} \propto \frac{\mu}{2}\left(1 \pm c^{(1)}\cos(\varphi)\right), \tag{6}$$

where $c^{(1)} = p_0 = \cos^2(\theta/2)$ for a state comprising only 0 or 1 photon. More generally, for pure photonic states of the form $|\Psi\rangle = \sum_{n=0}^{\infty}\sqrt{p_n}|n\rangle$, this quantity is

$$c^{(1)} = \frac{1}{\mu}\left|\sum_{n=0}^{\infty}\sqrt{(n+1)p_n p_{n+1}}\right|^2, \tag{7}$$

and it quantifies the mean first-order photon-number coherence between states containing n and $n+1$ photons. The oscillations in single counts reflect single-photon interference phenomena that take place between two indistinguishable emitted wave packets. Importantly, this interference effect invalidates the standard normalization procedures described in the previous section: those relying on the recorded single counts or on the areas of far delay peaks $|k| \geq 2$.

3.2. Normalization in the Presence of Coherence with Vacuum

In the presence of coherence with vacuum, Eq. (6) shows that in parallel configuration, the product $I_1 I_2$ depends on φ, and the areas of the $|k| \geq 2$ delay peaks are now given by

$$G^{(2)}_{D_1,D_2,\parallel}(|k| \geq 2) \propto 1 - \left(c^{(1)}\cos(\varphi)\right)^2. \tag{8}$$

This is a manifestation of first-order interference, similar to classical interference, where the interferometer phase causes fringes at the output that can increase the counts at one detector while decreasing the counts at the other. This results in an overall reduced coincidence count rate unless $\varphi = \pi/2$ exactly. As a consequence, when overlooking the presence of this type of quantum interference and having no control over the phase φ, the far delay peaks will be smaller than expected when $c^{(1)} \neq 0$. Hence, the normalization factor $\mu^2/4$, which should be independent of phase and coherent effects, can no longer be obtained from just the far delay peaks of the detector cross correlation histogram [26].

As a solution, one can access the normalization factor by recording both the cross and auto-correlation functions $G^{(2)}_{D_i,D_j}(t_1,t_2)$ with $i \neq j$ and $i = j$, respectively, considering that

$$\frac{\mu^2}{4} = \frac{1}{4}\left(G^{(2)}_{D_1,D_1}(k) + 2G^{(2)}_{D_1,D_2}(k) + G^{(2)}_{D_2,D_2}(k)\right), \tag{9}$$

with $|k| \geq 2$ and assuming parallel polarization. This normalization factor is also conveniently robust against efficiency imbalances in the interferometer (see Supplement 1).

Using this phase-independent and coherence-robust normalization procedure, we plot in Fig. 3(a) the normalized coincidence histograms in parallel (red) and orthogonal (grey) polarization configuration for $\theta = 0.22\pi$. We observe a strong suppression of the far delay peaks as anticipated by the proportionality in Eq. (8), here averaged over the fluctuating phase φ. We also perform phase-resolved intensity correlation measurements using time-tagging techniques, where we divide the data into separate normalized histograms depending on the instantaneous interferometer phase φ deduced from the detector single counts (see Supplement 1 for experimental details). Figure 3(b) shows the experimentally measured peak areas of the $|k| \geq 2$ delay peaks as a function of φ for various probed pulse areas

θ. An increasingly strong phase-dependence is observed as the vacuum component of the photonic state increases. These observations agree well with the theoretical prediction

$$g^{(2)}_{D_1,D_2,\|}(|k| \geq 2) = 1 - \left(c^{(1)} \cos(\varphi)\right)^2, \quad \textbf{(10)}$$

as illustrated in Fig. 3(c).

Conversely, we show in Supplement 1, experimentally and theoretically, that the normalized zero delay peak $g^{(2)}_{D_1,D_2,\|}(k = 0)$ exhibits no phase-dependence. One can thus use the standard relation (Eq. (4)) along with this phase-independent normalization procedure to extract the indistinguishability, even in the presence of coherence with vacuum.

We also analyze the area of the $|k| = 1$ peaks of the properly normalized histograms as shown in Fig. 3(d) which evidences strong phase dependence increasing with the vacuum component. When $\theta \simeq \pi$, we observe a normalized area close to 3/4, but for $\theta < \pi$, the peak areas can exhibit both lower and higher values. Through a complete theoretical analysis of the path-unbalanced interferometer including coherent effects (see Supplement 1), we find that the normalized $|k| = 1$ peak area is described by

$$g^{(2)}_{D_1,D_2,\|}(|k| = 1) = \frac{1}{4} + \frac{1}{2}\left(1 - s^{(2)}_{\{1|M\}} \cos(2\varphi)\right), \quad \textbf{(11)}$$

where the amplitude $s^{(2)}_{\{1|M\}}$ quantifies the joint temporal overlap between the first-order photon-number coherence $\langle \hat{a}(t) \rangle$ that dictates $c^{(1)}$, and the first-order two-time amplitude correlation $\langle \hat{a}^\dagger(t_1)\hat{a}(t_2) \rangle$ that dictates M. Similar to the $g^{(2)}$ notation, the superscript (2) in $s^{(2)}_{\{1|M\}}$ indicates here that this amplitude is a second-order correlation, i.e., a two-photon process. In the case of an emitter subject to pure dephasing only, we theoretically show that

$$s^{(2)}_{\{1|M\}} = c^{(1)} \left(\frac{2M}{1+M}\right). \quad \textbf{(12)}$$

Figure 3(e) illustrates the theoretically expected behavior for perfect single-photon indistinguishability ($M = 1$) as a function of pulse area θ and interferometer phase φ accurately accounting for our experimental observations.

The above observations and theoretical analysis evidence how the quantum interference of single wave packets on a beam splitter is modified in the presence of coherence with vacuum. In the next section, we discuss how these changes should be taken into account for accurate measurements of the indistinguishability of single-photon wave packets from quantum emitters.

4. ERRORS IN INDISTINGUISHABILITY MEASUREMENTS

Many quantum emitters are investigated as sources of indistinguishable photons (atoms, ions, semiconductor QDs, defects in 2D materials etc.) [45]. When pursuing the generation of indistinguishable photons, coherent control schemes are naturally adopted as they ensure the lowest degree of time jitter for the spontaneous emission process.

Due to its relatively recent evidence [24], the presence of photon-number coherence in the emission of resonantly excited atoms or artificial atoms has been widely ignored so far. As a result, the influence of optical phases in the experimental apparatus that play an important role in the presence of coherence with vacuum (see Section 3) has been completely overlooked. Importantly, we underline that such phase-resolved analysis would add a great level of complexity to the experimental study, requiring active phase-stabilization or high photon collection efficiency to trace the phase effect as it varies within the measurement time, as well as event timing to access auto-correlation signals. Still, we show now that there is actually a simple way to identify the presence of photon-number coherence in standard experimental studies of photon indistinguishability, which allows to trace back errors in its estimation.

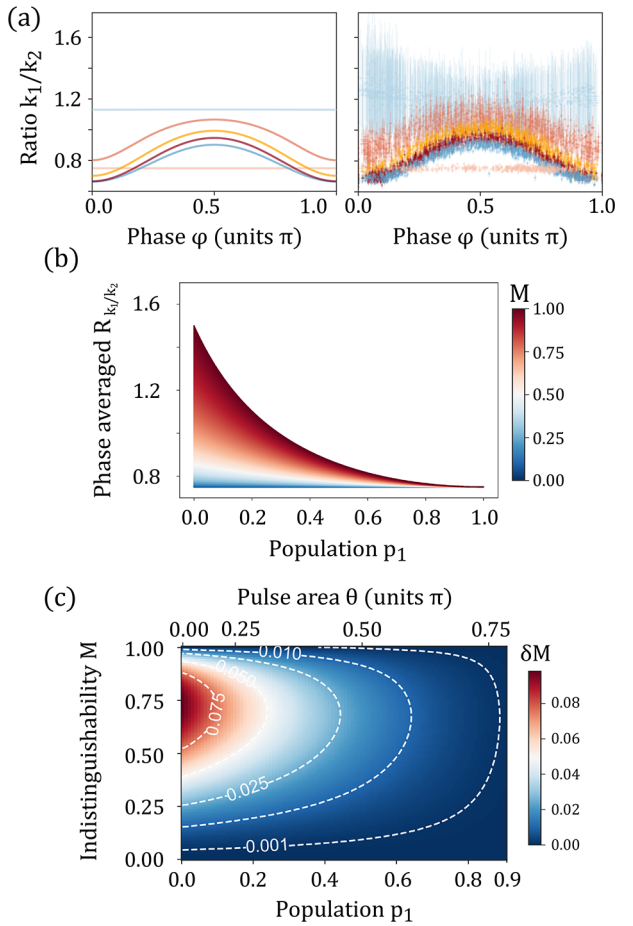

Fig. 4. (a) Ratio of the normalized $|k| = 1$ and $|k| \geq 2$ peak areas (left, theoretical; right, experimental) as a function of optical phase φ for different pulse areas θ. The colors follow the same color map as in Fig. 3. (b) Phase averaged peak ratios of the normalized $|k| = 1$ and $|k| \geq 2$ peak areas as a function of excited state population p_1 and indistinguishability M (color coded) for a purely dephased emitter. (c) Error in indistinguishability δM as a function of pulse area θ (or p_1) and single-photon indistinguishability M considering a purely dephased emitter.

We consider the ratio R_{k_1/k_2} of the $|k| = 1$ and $|k| \geq 2$ peak areas. In Fig. 4(a), we plot this ratio as a function of the interferometer phase φ for both the theoretical prediction and our experimental data, once again illustrating good agreement between the two. If the measurements are not phase-resolved but phase-averaged, $\cos(2\varphi)$ in Eq. (11) vanishes and $\cos^2(\varphi)$ in Eq. (10) tends to 1/2. Thus, the ratio becomes $R_{k_1/k_2} = 3/(4 - 2(c^{(1)})^2)$ and $R_{k_1/k_2} > 3/4$ implies that $c^{(1)} > 0$, hence indicating the presence of first-order coherence. We also note that this technique to measure $c^{(1)}$ can work even if the source has non-negligible multi-photon emission by applying a minor correction to R_{k_1/k_2}.

Table 1. Estimated Ratio R_{k_1/k_2} in a Selection of Prior Publications Resulting in an Estimation for the Vacuum Component p_0 and Errors on Indistinguishability

Emitter	Ref.	Reported V_{HOM}	R_{k_1/k_2}	p_0	δM
QD	[46]	(89.2 ± 0.9)%	0.90 ± 0.06	40%	1%
QD	[47]	(91.1 ± 1.9)%	0.80 ± 0.04	30%	0.5%
QD	[48]	(92.6 ± 1.6)%	0.97 ± 0.04	55%	1.5%
QD	[49]	(93.0 ± 1.3)%	1.04 ± 0.04	60%	1.5%
QD	[50]	(95 ± 4)%	0.88 ± 0.04	30%	0.5%
Ion	[51]	(80 ± 4)%	0.86 ± 0.02	30%	0.5%

Figure 4(b) shows the theoretically calculated ratio assuming phase averaging and a purely dephased emitter as a function of θ for various M, evidencing a correspondence between the measured ratio and the fraction of coherent vacuum in the photon state. We can thus give an estimation for the population of coherent vacuum contributing to previous measurements in the literature. As an example, we have gathered in Table 1 the ratio R_{k_1/k_2} estimated from experimental data from some works [46–51], where a clear deviation from the 3/4 value is observed. We deduce the corresponding estimation of vacuum population present (columns 4 and 5) illustrating how ignoring the presence of coherence with vacuum has led to errors in the derived indistinguishability values. Interestingly, the errors lead to an underestimation of the photon indistinguishability.

Figure 4(c) shows the calculated error δM as a function of pulse area θ for the phase-averaged scenario. Here, our study is limited to the case where the two-photon component is negligible, typically for values p_1<0.9. We define this error in indistinguishability as $\delta M = M - V_{HOM}$, where we consider M the single-photon indistinguishability and V_{HOM} the indistinguishability extracted from coincidence histograms using the areas of the far delay peaks as a reference. A tentative estimation of the errors in the literature is shown in the last column of Table 1. These errors appear small, but we underline that every fraction of a percent is critical when optimizing the indistinguishability of source emission—a requirement for fault tolerant quantum information processing.

Note that we have so far focused our study on the coherence between the zero- and one-photon components, which holds below π-pulse and for short enough excitation pulses. However, it is important to emphasize that the above-described effects can also occur close to and beyond $\theta = \pi$, where the first-order photon-number coherence may appear between higher photon-number components following Eq. (7). Figure 2(a) shows the theoretical predictions of the vacuum probability p_0 and the one- p_1 and two-photon contribution $2p_2$ along the Rabi curve upon resonant excitation with a finite pulse of 7-ps duration and an emission decay time of approximately 161 ps. The two-photon component (dash-dotted line) is expected to be significantly larger than the zero-photon component at $\theta = \pi$. This effect still results in a non-zero first-order coherence at maximum excited-state population (i.e., maximal brightness of the source), mainly dictated by the coherence between the one- and two-photon component according to Eq. (7). Experimentally, we indeed witness the presence of photon-number coherence in anti-correlated oscillations in the single counts, see Supplemental Fig. S2. Thus, corrections to indistinguishability measurements must also be implemented at the highest brightness of the source, i.e., around $\theta = \pi$ by including the analysis of the emitted state up to two photons.

5. ENTANGLEMENT IN PARTIAL MEASUREMENTS

In this section, we discuss the quantum phenomena behind the observation of phase-dependent single counts (see Fig. 2(c)). We show that it arises from partial photonic measurements and reveals the presence of spatiotemporal entanglement.

We first consider the events leading to a coincidence for $|k| = 1$ in the unbalanced Mach–Zehnder interferometer with a delay line ($\tau = \tau_p$) implemented in one of the arms. In the high loss regime, a $|k| = 1$ coincidence count implies the detection of exactly two photons, one at each detector and separated in time by τ_p in an early and late detection bin. Figure 5(a) shows the pulse sequence arriving at the first beam splitter of the Mach–Zehnder interferometer that contribute to this signal—each pulse at the input of the interferometer is a quantum superposition of 0 and 1 photon (Eq. (5)). Labeling $|U\rangle_{e,l}$ and $|L\rangle_{e,l}$, a single-photon arriving from the upper (U) and lower (L) input of the last beam splitter, in early (e) or late (l) detection time bins, there are four states of light impinging on BS_2 that lead to a two-photon coincidence count contributing to $g^{(2)}_{D_1,D_2,\|}(|k| = 1)$: $|U\rangle_e|U\rangle_l$, $|U\rangle_e|L\rangle_l$, $|L\rangle_e|U\rangle_l$, and $|L\rangle_e|L\rangle_l$, see Fig. 5(b). The case $|U\rangle_e|L\rangle_l$, however, can only result from light pulses containing

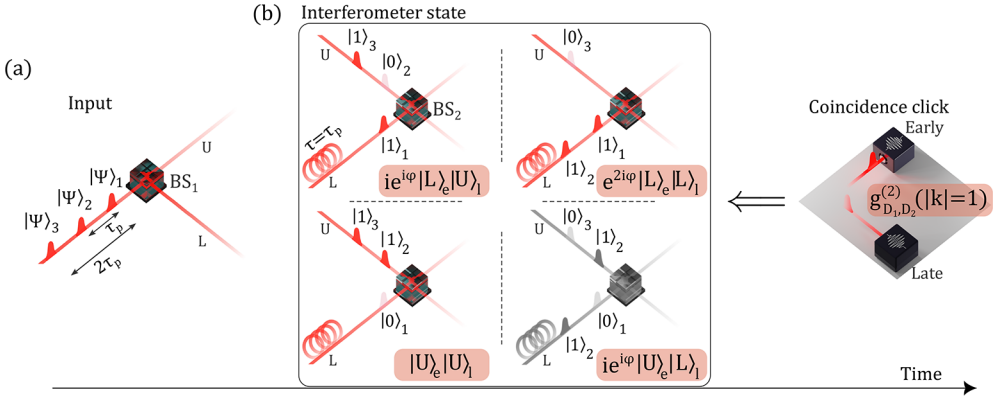

Fig. 5. (a) Considered input to the unbalanced Mach–Zehnder interferometer. Here, U and L denote the upper and lower path of the interferometer. (b) Detection of $g^{(2)}_{D_1,D_2,\|}(|k| = 1)$ coincidence clicks (separated in time by $\tau = \tau_p$) projects the interferometer state into the path and time entangled state shown on the left (at the interfering beam splitter BS_2). The subscripts e, l denote early and late detection, respectively. The state of light $ie^{i\varphi}|U\rangle_e|L\rangle_l$ inside the interferometer can only be produced by an input state involving two photons in one pulse, and hence it has a negligible chance of occurring. See main text for details.

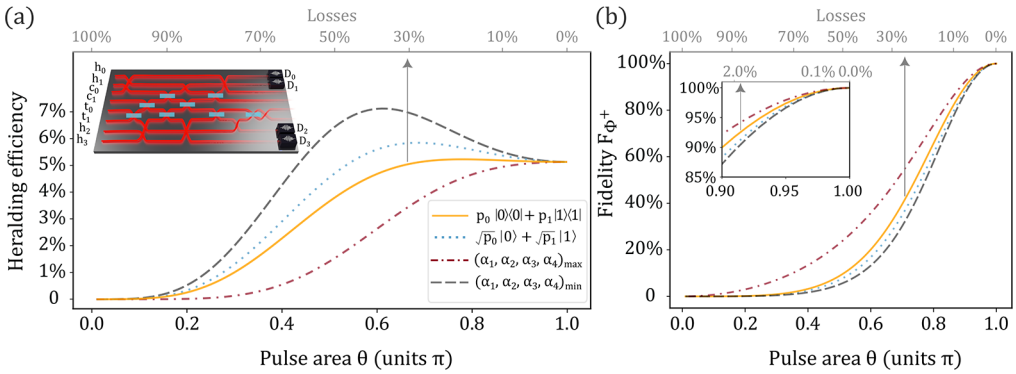

Fig. 6. (a) Heralding efficiency and (b) fidelity with respect to the Bell state $|\Phi^+\rangle$ as a function of pulse area θ of the driving field generating the photonic states input to the heralded CNOT gate (inset) where the target (t), control (c) paths encode logical qubits, and certain combinations of detector clicks at the output of the heralding (h) paths signal a successful gate [53]. The different curves correspond to different scenarios: where physical input states share the same phase, $\alpha = 0$ (blue, dotted), where α is optimized to obtain maximum fidelity (red, dash-dotted), and where α corresponds to a minimized gate fidelity (grey, dashed). Also shown are the heralding efficiency and fidelity as a function of losses (yellow, solid).

more than one photon: a situation that has a negligible chance of occurring in our experiment and so we disregard it.

If the remaining three cases are indistinguishable, the detection of $|k| = 1$ coincidences actually projects the state of light entering BS_2 onto the partially path-entangled state:

$$|\Psi\rangle = \frac{1}{\sqrt{3}}\left(ie^{i\varphi}|L\rangle_e|U\rangle_l + |U\rangle_e|U\rangle_l - e^{2i\varphi}|L\rangle_e|L\rangle_l\right), \quad \textbf{(13)}$$

a state with an entanglement concurrence of $C = 2/3$ [52]. In practice, photon losses and photon distinguishability will cause these states to become partially distinguishable, which reduces the amount of path entanglement and hence reduces the visibility of oscillations in the $|k| = 1$ peak areas. For example, a three-photon state followed by the loss of a single photon could produce the outcome $|L\rangle_e|U\rangle_l$ while being completely distinguishable from the other two cases via the lost photon (see Supplement 1).

We find that the amplitude $s^{(2)}_{\{1|M\}}$, quantifying the visibility of the $|k| = 1$ coincidences, is related to the entanglement concurrence of this path-entangled state entering BS_2, according to $C = (2/3)s^{(2)}_{\{1|M\}}$. The observation of phase-dependent areas of the $|k| = 1$ peaks thus reveals the generation of spatiotemporal entanglement with a maximal concurrence of 2/3 when θ tends to zero and M to one, which conversely vanishes when approaching $\theta = \pi$.

6. EFFECT ON HERALDED GATES

Based on the above study of HOM interference, we are now in a position to reach some general understanding about the impact of coherence with vacuum on linear quantum protocols. Starting from N pulses containing quantum superpositions of zero and one photons, we expect no modification of linear quantum processing protocols when detecting N single photons. In such a case, the measurement post-selects on all pulses being in the Fock state 1. However, large scale linear quantum computing relies on partial measurement of photons and feed-forward. In such a case, by measuring only n photons out of N pulses, one does not post-select on a single configuration, but on multiple interfering quantum trajectories where the n photons come from different pulses. Such additional quantum interferences will modify the operation of any heralded protocol differently from the presence of photon loss (incoherent vacuum).

To illustrate this effect, we consider the case of the heralded CNOT gate [53] in the path encoded implementation of Ref. [54], see inset in Fig. 6(a). This gate requires four ancillary modes (h) to implement the nonlinearity and herald the successful operation on the control (c) and target (t) qubit. The gate is heralded by the detection of exactly one photon at detectors D_1 and D_3, and zero photons at detectors D_0 and D_2. If the qubits are prepared in the logical state $|\psi_{in}\rangle = \frac{1}{\sqrt{2}}(|0_l\rangle_c + |1_l\rangle_c) \otimes |0_l\rangle_t$, the output logical state is a maximally entangled Bell state $|\Phi^+\rangle = (|0_l\rangle_c|0_l\rangle_t + |1_l\rangle_c|1_l\rangle_t)/\sqrt{2}$. The heralding probability, in the ideal case where none of the four photons gets lost, is $P_{(h|4)} = (11 - 6\sqrt{2})/49$, or approximately 5.1% [54].

To model the effect of coherence with vacuum on the operation of this gate, we perform numerical simulations using the Perceval framework [55]. We first calculate the heralding efficiency $P_{(h)}$ considering incoherent losses, i.e., considering input states in the form of $\psi'(\theta) = p_0|0\rangle\langle 0| + p_1|1\rangle\langle 1| = \cos^2(\theta/2)|0\rangle\langle 0| + \sin^2(\theta/2)|1\rangle\langle 1|$ (solid yellow curve in Fig. 6(a), and corresponding upper x-axis). We then consider the case of a quantum superposition of 0 and 1 photons. All four input single-photon states are initially prepared in the same state $|\Psi(\theta, \alpha = 0)\rangle$ (according to Eq. (5)) and we plot the corresponding heralding efficiency (dotted blue curve).

We find that the maximal heralding efficiency can be increased from 5.1% at $\theta = \pi$ to 5.8% for a certain pulse area of $\theta < \pi$. This observation can be understood considering that coherence with vacuum leads to additional interference effects when the number of measurements is lower than the number of manipulated light pulses. As observed on the single counts and on the $|k| = 1$ peaks in the HOM experiment, it can either reduce or increase the amplitude at certain outputs such that $P_{(h)}$ can be increased or decreased compared with the case of incoherent vacuum. Actually, by numerically exploring $P_{(h)}$ when varying individually the four phases $(\alpha_1, \alpha_2, \alpha_3, \alpha_4)$ of the four input states $|\Psi(\theta, \alpha)\rangle$, we find that $P_{(h)}$ can span anywhere from 2.5% up to 7.1% at $\theta = 0.6\pi$ (dashed and dash-dotted curves).

Conversely, Fig. 6(b) shows that the fidelity F of the output state $|\psi_{out}\rangle$, with respect to the ideal Bell state, is decreased when the four light states are in the input state $|\Psi(\theta, \alpha = 0)\rangle$ (dotted

blue) compared with the case of equivalent incoherent vacuum. Symmetrically, for the phase combination (α_1, α_2, α_3, α_4) that maximizes (minimizes) the heralding efficiency, we find that the fidelity of the heralded state is decreased (increased) compared with incoherent losses. This behavior can be understood considering that errors arise only from additional vacuum components in the input (either coherent or incoherent). As a result, an enhanced heralding efficiency with respect to incoherent loss arising from quantum interference necessarily reduces the probability of obtaining two photons at the logical outputs.

Quantitatively, the gate operates perfectly ($F = 100\%$) with conditional probability $P_{(h|4)}$, i.e., a heralding signal was observed given that the input state contains exactly four photons, while $F = 0\%$ if the input state contains fewer than four photons. In the case of either coherent or incoherent loss, this implies that the scheme will operate as expected only with probability $P_{(4)} = {p_1}^4$, where $p_1 = \sin^2(\theta/2)$. Prior to heralding, the fidelity of the output state thus depends only on the probability of having four photons at the input $P_{(4)}$ and the ideal gate heralding probability $P_{(h|4)}$. As such, the fidelity post-heralding is simply the probability $P_{(4|h)}$ of having had four photons given that a heralding signal was observed. Thus, using Bayes' theorem, we get

$$F = \frac{P_{(4)}P_{(h|4)}}{P_{(h)}}, \tag{14}$$

where $P_{(h)}$ is the only term depending on the photon-number coherence and relative phases of the superposition with vacuum.

It is interesting to note that any suppression of the heralding efficiency $P_{(h)}$, stemming from coherence, acts as a filter to reduce the occurrence of erroneous output states that contain fewer than two photons, thereby enhancing the heralded Bell-state fidelity overall. Likewise, any enhancement of $P_{(h)}$ increases the number of erroneous output states, leading to a reduction in the fidelity.

7. CONCLUSION

We have shown that the photon-number coherence naturally present in the light wave packets generated by quantum emitters leads to a large variety of quantum interference phenomena and entanglement. They impact both the standard techniques employed in the development of deterministic quantum light sources and information processing with photons. Starting with an experimental configuration as simple as the Hong–Ou–Mandel interferometer, we have shown that the long standardized protocol to deduce the photon indistinguishability from quantum emitters needs to be revised.

In the broader context of quantum information processing in the discrete variable framework, i.e., exploiting single-photon wave packets, our study shows that the absence of a photon cannot simply be treated as a photon loss as has been done so far in the discrete variable paradigm community. In particular, we experimentally demonstrate that the presence of photon-number coherence can be a resource to create entanglement in an unbalanced Mach–Zehnder interferometer, which touches on fundamental relationships in quantum physics [56]. As another example, we have found that coherence with vacuum can actually lead to reduced errors for a photonic CNOT gate compared with incoherent vacuum when leveraging control over the phase of the coherent superposition. This hints that the amount and form of quantum coherence plays an important role in determining the performance of quantum information processing. Such a general relationship may be better elucidated from the perspective of resource theory [57]. We anticipate that the possibility to deterministically generate quantum superpositions of zero and one photon in a fully controlled manner with quantum emitters opens up many possibilities for photon-based quantum information processing, providing additional degrees of freedom to leverage single-rail qubit encoding in a revisited way for exploitation. It also may provide a critical bridge between continuous- and discrete-variable paradigms of quantum information processing.

Funding. Agence Nationale de la Recherche (QuDICE, ANR-22-PETQ-0011, ANR-22-PETQ-0006); Comunidad de Madrid (Atracción de Talento,365 Mod. 1); Ministerio de Ciencia e Innovación (PID2020113445-GB-I00); Fundación Ramón Areces (ULTRA-BRIGHT).

Acknowledgment. This work was partially supported by the Paris Ile-de-France Région in the framework of DIM SIRTEQ, the European Union's Horizon 2020 FET OPEN project PHOQUSING (Grant ID 862035), Horizon CL4 program under the grant agreement 101135288 for EPIQUE project, by the European Commission as part of the EIC accelerator program under the grant agreement 190188855 for SEPOQC project, the Plan France 2030 through the projects ANR22-PETQ-0011, ANR-22-PETQ-0006 and ANR-22-PETQ-0013, the French National Research Agency (ANR) project QU-DICE (ANR-18-CE47-0009). This work was done within the C2N micro nanotechnologies platforms and partly supported by the RENATECH network and the General Council of Essonne. C.A.S. acknowledges Comunidad de Madrid (Atracción de Tal- ento,365 Mod. 1), Ministerio de Ciencia e Innovación (PID2020113445- GB-I00), and Fundación Ramón Areces (ULTRA-BRIGHT).

Disclosures. The authors declare no conflicts of interest.

Data availability. Correspondence and requests for data should be addressed to I.M.d.B.W. (imaillet@ic.ac.uk) or P.S. (pascale.senellart-mardon@c2n.upsaclay.fr).

Supplemental document. See Supplement 1 for supporting content.

REFERENCES

1. A. Kuhn, M. Hennrich, and G. Rempe, "Deterministic single-photon source for distributed quantum networking," Phys. Rev. Lett. **89**, 067901 (2002).
2. J. McKeever, A. Boca, A. D. Boozer, *et al.*, "Deterministic generation of single photons from one atom trapped in a cavity," Science **303**, 1992–1994 (2004).
3. A. Sipahigil, K. D. Jahnke, L. J. Rogers, *et al.*, "Indistinguishable photons from separated silicon-vacancy centers in diamond," Phys. Rev. Lett. **113**, 113602 (2014).
4. A. Kiraz, M. Ehrl, T. Hellerer, *et al.*, "Indistinguishable photons from a single molecule," Phys. Rev. Lett. **94**, 223602 (2005).
5. H. G. Barros, A. Stute, T. E. Northup, *et al.*, "Deterministic single-photon source from a single ion," New J. Phys. **11**, 103004 (2009).
6. N. Somaschi, V. Giesz, L. De Santis, *et al.*, "Near-optimal single-photon sources in the solid state," Nat. Photonics **10**, 340–345 (2016).
7. N. Tomm, A. Javadi, N. O. Antoniadis, *et al.*, "A bright and fast source of coherent single photons," Nat. Nanotechnol. **16**, 399–403 (2021).
8. C. Santori, D. Fattal, J. Vuckovic, *et al.*, "Single-photon generation with InAs quantum dots," New J. Phys. **6**, 89 (2004).
9. A. J. Bennett, D. C. Unitt, A. J. Shields, *et al.*, "Influence of exciton dynamics on the interference of two photons from a microcavity single-photon source," Opt. Express **13**, 7772–7778 (2005).
10. S. Weiler, A. Ulhaq, S. M. Ulrich, *et al.*, "Highly indistinguishable photons from a quantum dot in a microcavity," Phys. Status Solidi B **248**, 867–871 (2011).
11. R. Teets, J. Eckstein, and T. W. Hänsch, "Coherent two-photon excitation by multiple light pulses," Phys. Rev. Lett. **38**, 760–764 (1977).

12. A. Reigue, J. Iles-Smith, F. Lux, *et al.*, "Probing electron-phonon interaction through two-photon interference in resonantly driven semiconductor quantum dots," Phys. Rev. Lett. **118**, 233602 (2017).
13. Z. X. Koong, E. Scerri, M. Rambach, *et al.*, "Coherent dynamics in quantum emitters under dichromatic excitation," Phys. Rev. Lett. **126**, 047403 (2021).
14. J. Liu, R. Su, Y. Wei, *et al.*, "A solid-state source of strongly entangled photon pairs with high brightness and indistinguishability," Nat. Nanotechnol. **14**, 586–593 (2019).
15. P. Senellart, G. Solomon, and A. White, "High-performance semiconductor quantum-dot single-photon sources," Nat. Nanotechnol. **12**, 1026–1039 (2017).
16. J. L. O'Brien, "Optical quantum computing," Science **318**, 1567–1570 (2007).
17. H. Wang, J. Qin, X. Ding, *et al.*, "Boson sampling with 20 input photons and a 60-mode interferometer in a 10^{14}-dimensional Hilbert space," Phys. Rev. Lett. **123**, 250503 (2019).
18. N. Maring, A. Fyrillas, M. Pont, *et al.*, "A versatile single-photon-based quantum computing platform," Nat. Photonics **18**, 603–609 (2024).
19. Y. Karli, D. A. Vajner, F. Kappe, *et al.*, "Controlling the photon number coherence of solid-state quantum light sources for quantum cryptography," npj Quantum Inf **10**, 17 (2024).
20. G. Rodari, F. Hoch, A. Suprano, *et al.*, "Polarization-encoded photonic quantum-to-quantum Bernoulli factory based on a quantum dot source," Sci. Adv. **10**, 1 (2024).
21. B. Polacchi, F. Hoch, G. Rodari, *et al.*, "Quantum teleportation of a genuine vacuum-one-photon qubit generated via a quantum dot source," arXiv, (2023).
22. L. Carosini, V. Oddi, F. Giorgino, *et al.*, "Programmable multiphoton quantum interference in a single spatial mode," Sci. Adv. **10**, 1 (2024).
23. H. Cao, L. Hansen, F. Giorgino, *et al.*, "Photonic source of heralded Greenberger-Horne-Zeilinger states," Phys. Rev. Lett. **132**, 130604 (2024).
24. J. C. Loredo, C. Antón, B. Reznychenko, *et al.*, "Generation of nonclassical light in a photon-number superposition," Nat. Photonics **13**, 803–808 (2019).
25. For simplicity, we describe our system in the following as an effective two-level system with instantaneous state preparation, implying $g^{(2)}(0) = 0$.
26. This normalisation method is also incorporated as a standard feature in Ref. [44].
27. D. W. Berry, A. I. Lvovsky, and B. C. Sanders, "Interconvertibility of single-rail optical qubits," Opt. Lett. **31**, 107 (2006).
28. D. Drahi, D. V. Sychev, K. K. Pirov, *et al.*, "Entangled resource for interfacing single- and dual-rail optical qubits," Quantum **5**, 416 (2021).
29. Y. Liu, T.-Y. Chen, L.-J. Wang, *et al.*, "Experimental measurement-device-independent quantum key distribution," Phys. Rev. Lett. **111**, 130502 (2013).
30. A. Rubenok, J. A. Slater, P. Chan, *et al.*, "Real-world two-photon interference and proof-of-principle quantum key distribution immune to detector attacks," Phys. Rev. Lett. **111**, 130501 (2013).
31. H.-K. Lo, M. Curty, and B. Qi, "Measurement-device-independent quantum key distribution," Phys. Rev. Lett. **108**, 130503 (2012).
32. D. T. Pegg, L. S. Phillips, and S. M. Barnett, "Optical state truncation by projection synthesis," Phys. Rev. Lett. **81**, 1604–1606 (1998).
33. S. A. Babichev, B. Brezger, and A. I. Lvovsky, "Remote preparation of a single-mode photonic qubit by measuring field quadrature noise," Phys. Rev. Lett. **92**, 047903 (2004).
34. D. W. Berry, A. I. Lvovsky, and B. C. Sanders, "Efficiency limits for linear optical processing of single photons and single-rail qubits," J. Opt. Soc. Am. B **24**, 189 (2007).
35. M. Bozzio, M. Vyvlecka, M. Cosacchi, *et al.*, "Enhancing quantum cryptography with quantum dot single-photon sources," npj Quantum Inf **8**, 104 (2022).
36. J. J. Renema, "Simulability of partially distinguishable superposition and Gaussian boson sampling," Phys. Rev. A **101**, 063840 (2020).
37. V. Giesz, N. Somaschi, G. Hornecker, *et al.*, "Coherent manipulation of a solid-state artificial atom with few photons," Nat. Commun. **7**, 1 (2016).
38. A. M. Barth, S. Lüker, A. Vagov, *et al.*, "Fast and selective phonon-assisted state preparation of a quantum dot by adiabatic undressing," Phys. Rev. B **94**, 045306 (2016).
39. M. Cosacchi, F. Ungar, M. Cygorek, *et al.*, "Emission-frequency separated high quality single-photon sources enabled by phonons," Phys. Rev. Lett. **123**, 017403 (2019).
40. S. E. Thomas, M. Billard, N. Coste, *et al.*, "Bright polarized single-photon source based on a linear dipole," Phys. Rev. Lett. **126**, 233601 (2021).
41. R. Trivedi, K. A. Fischer, J. Vučković, *et al.*, "Generation of non-classical light using semiconductor quantum dots," Adv. Quantum Technol. **3**, 1900007 (2020).
42. H. Ollivier, S. E. Thomas, S. C. Wein, *et al.*, "Hong-Ou-Mandel interference with imperfect single photon sources," Phys. Rev. Lett. **126**, 1–9 (2021).
43. J. C. Loredo, N. A. Zakaria, N. Somaschi, *et al.*, "Scalable performance in solid-state single-photon sources," Optica **3**, 433–440 (2016).
44. Swabian Instruments 'Time Tagger User Manual,' Release 2.17. 4.0 (2024), https://www.swabianinstruments.com/static/downloads/TimeTagger_User_Manual.pdf.
45. I. Aharonovich, D. Englund, and M. Toth, "Solid-state single-photon emitters," Nat. Photonics **10**, 631–641 (2016).
46. B. Da Lio, C. Faurby, X. Zhou, *et al.*, "A pure and indistinguishable single-photon source at telecommunication wavelength," Adv. Quantum Technol. **5**, 2200006 (2022).
47. Y.-M. He, J. Liu, S. Maier, *et al.*, "Deterministic implementation of a bright, on-demand single-photon source with near-unity indistinguishability via quantum dot imaging," Optica **4**, 802–808 (2017).
48. C. Matthiesen, M. Geller, C. H. H. Schulte, *et al.*, "Phase-locked indistinguishable photons with synthesized waveforms from a solid-state source," Nat. Commun. **4**, 1600 (2013).
49. S. Gerhardt, M. Deppisch, S. Betzold, *et al.*, "Polarization-dependent light-matter coupling and highly indistinguishable resonant fluorescence photons from quantum dot-micropillar cavities with elliptical cross section," Phys. Rev. B **100**, 115305 (2019).
50. Y. Karli, D. A. Vajner, F. Kappe, *et al.*, "Controlling the photon number coherence of solid-state quantum light sources for quantum cryptography," arXiv (2023).
51. S. Ourari, L. Dusanowski, S. P. Horvath, *et al.*, "Indistinguishable telecom band photons from a single Er ion in the solid state," Nature **620**, 977–981 (2023).
52. W. K. Wootters, "Entanglement of formation and concurrence," Quantum Info. Comput. **1**, 27–44 (2001).
53. E. Knill, R. Laflamme, and G. J. Milburn, "A scheme for efficient quantum computation with linear optics," Nature **409**, 46–52 (2001).
54. R. Okamoto, J. L. O'Brien, H. F. Hofmann, *et al.*, "Realization of a Knill-Laflamme-Milburn controlled-NOT photonic quantum circuit combining effective optical nonlinearities," Proc. Natl. Acad. Sci. U.S.A. **108**, 10067–10071 (2011).
55. N. Heurtel, A. Fyrillas, G. de Gliniasty, *et al.*, "Perceval: a software platform for discrete variable photonic quantum computing," Quantum **7**, 931 (2023).
56. N. Killoran, F. Steinhoff, and M. Plenio, "Converting nonclassicality into entanglement," Phys. Rev. Lett. **116**, 080402 (2016).
57. T. Baumgratz, M. Cramer, and M. Plenio, "Quantifying coherence," Phys. Rev. Lett. **113**, 140401 (2014).